Journal of Materials Chemistry A

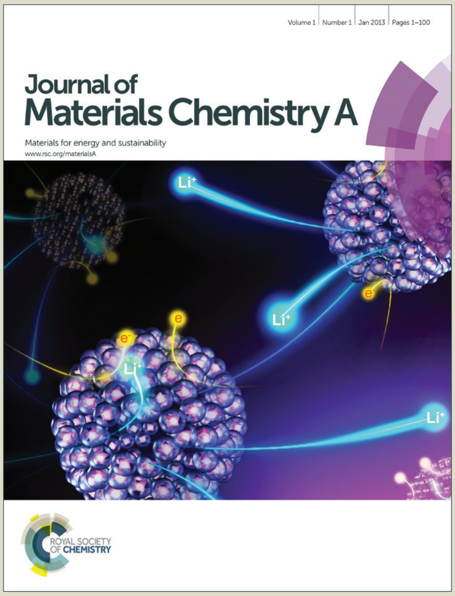

ROYAL SOCIETY OF CHEMISTRY

www.rsc.org/materialsA

Three-dimensional $Co_3O_4@C@Ni_3S_2$ Sandwich-Structured Nanoneedle Arrays: Towards High-Performance Flexible All-Solid-State Asymmetric Supercapacitors

Dezhi Kong,[ab] Chuanwei Cheng,*[a] Ye Wang,[b] Jen It Wong,[b] Yaping Yang[a] and Hui Ying Yang*[b]

[a]*Shanghai Key Laboratory of Special Artificial Microstructure Materials and Technology, School of Physics Science and Engineering, Tongji University, Shanghai 200092, P.R. China*

[b]*Pillar of Engineering Product Development, Singapore University of Technology and Design, 8 Somapah Road, Singapore 487372*

Abstract

In this paper, we report the design and fabrication of a novel hierarchical $Co_3O_4@C@Ni_3S_2$ sandwich-structured nanoneedle arrays (NNAs) electrode for supercapacitor application. The supercapacitor performance based on the $Co_3O_4@C@Ni_3S_2$ NNAs electrodes are investigated in detail. A lightweight and flexible asymmetric supercapacitor (ASCs) is successfully fabricated using the $Co_3O_4@C@Ni_3S_2$ NNAs as the positive electrode and activated carbon (AC) as the negative electrode, which delivers an output voltage of 1.8 V, and high energy/power density (1.52 mWh cm^{-3} at 6 W cm^{-3} and 0.920 mWh cm^{-3} at 60 W cm^{-3}), as well as remarkable cycling stability (~91.43% capacitance retention after 10000 cycles), owing to the unique 3D porous sandwich-structured nanoneedle array architecture and a rational combination of the three electrochemically active materials. As a result, the ternary hybrid architectural design demonstrated in this study provides a new approach to fabricate high-performance metal oxides/sulfides composites nanostructure arrays for next-generation energy storage devices.

Keywords: $Co_3O_4@C@Ni_3S_2$, sandwich-structure, nanoneedle arrays, hierarchical, asymmetric supercapacitor

---

* To whom correspondence should be addressed: E-mail: [a] cwcheng@tongji.edu.cn or [b] yanghuiying@sutd.edu.sg

1. Introduction

Supercapacitors (SCs), also called electrochemical capacitors, are gaining intensive interests because of their desirable properties such as high power density (>10 kW kg^{-1}), fast charge/discharge rate (within seconds), long lifespan (>10^{5} cycles), and excellent safety.[1-5] With characteristics complementary to fuel cells and rechargeable batteries, SCs have been widely used in power grids, memory back-up systems, electric vehicles, and aerospace electronics.[6-8] However, further applications are hampered by the limited energy density. Therefore, it is highly desirable to develop high performance SCs with high energy density without sacrificing the power density and cycling stability. [9-11] Currently, two typical routes are developed to enhance the energy density of the SCs. One way is use of asymmetric supercapacitors (ASCs) that usually employ pseudo-capacitive materials and electric double-layer capacitive materials as positive and negative electrode, respectively, to provide a wider potential window, as a result of enhancing the energy density [12, 13]. Another way is to boost the capacitance by selection of proper electrode materials with nanostructured design. [14, 15]

Among the multitudinous available pseudo-capacitive materials, metal oxides and metal sulfides are two typical category of electrode materials, due to their excellent intrinsic properties and good electrochemical performance.[16-19] In particular, Co_3O_4 and Ni_3S_2 with high theoretical specific capacitance, low fabrication cost and environ-mentally friendly nature have been well investigated for pseudocapacitors.[20-25] However, the Co_3O_4 usually suffers from poor capacity retention and rate capacity, and the practical use of Ni_3S_2 as electrode materials is largely constrained by its poor electrical conductivity, which limit the charge-discharge rate of the supercapacitors.[25, 26] To address these problems, one way is design of composites by using highly conductive materials (e.g., carbon-based materials, metals, and metal oxides) as conductive backbones for supporting Ni_3S_2 nanostructured layer to enhance the performance.[27-29] Recently, the 3D hierarchical metal-oxides/Ni_3S_2 composite nanostructures with a smart design were reported to improve the electrochemical performance by the synergistic effects between the two components. For instances, Wang et al.[30] reported a novel heterogeneous core-shell structure by electrodepositing Ni_3S_2 nanosheets on hierarchical $NiCo_2O_4$ mesoporous nanothorn arrays on Ni foam, which demonstrated a higher specific capacitance (1716 F g^{-1} at 1 A g^{-1}) and a better rate capability (1104 F g^{-1} at 20 A g^{-1}) while maintaining 83.7% capacity after 2000 cycles. Xing et al.[31] demonstrated the electrodeposition of Ni_3S_2 on ZnO (ZnO@Ni_3S_2) arrays supported on Ni foam, which exhibited a very high specific capacitance of 1529 F g^{-1} at a current density of 2 A g^{-1}, good rate capability and cycling stability. Nevertheless, the fabrication route for 3D hierarchical metal oxides/sulfides is still rare and development of high-performance Ni_3S_2-based composites electrode remains a great challenge.

Herein, we demonstrate a novel and cost-effective approach to design and fabricate hierarchical Co_3O_4@C@Ni_3S_2 sandwich-structured nanoneedle arrays on Ni foam as a binder-free electrode for high-performance supercapacitors. The Co_3O_4@C@Ni_3S_2 nanostructure is composed of mesoporous Co_3O_4 arrays served as core, an ultrathin layer of small carbon nanoparticles film used as the inner shell layer and ultrathin Ni_3S_2 nanoflakes as the outer shell layer. This novel electrode design processes the following advantages. First, Co_3O_4 nanoneedles with well-defined single-crystalline nanostructure serve as both the backbone and conductive connection for Ni_3S_2, and its porous feature can enlarge the specific surface area. Moreover, ultrathin nanosheets-like Ni_3S_2 can increase the contact area with electrolyte, enable fast redox reaction, and protect the inner structure of Co_3O_4 as result of improving the durability. Second, the ultrathin layer of carbon NPs on the Co_3O_4 nanoneedle surfaces acts as an intermediate layer, which can not only provide electron “superhighways” for charge storage and transportation, but also act as a “protection” layer to induce a perfect coating of ultrathin Ni_3S_2 nanoflakes on the Co_3O_4 nanoneedle arrays. Third, the 3D Co_3O_4@C@Ni_3S_2 NNAs are directly growing on the conductive Ni foams providing excellent electrical contact, which would let each Co_3O_4@C@Ni_3S_2 involving in electrochemical reactions. By virtue of the synergetic contribution from individual constituents and the complex configuration, the resulting Co_3O_4@C@Ni_3S_2 NNAs electrode exhibit a much higher area capacitance (3.564 F cm^{-2}) than that of pristine Co_3O_4 nanoneedle arrays and Ni_3S_2 nanoflakes. Moreover, an asymmetric solid supercapacitor with the Co_3O_4@C@Ni_3S_2 NNAs as the positive electrode and activated carbon (AC) as the negative electrode delivers an energy density of 0.920 mWh cm^{-3} with a maximum power density of 60 W cm^{-3}.

2. Experimental Section

Synthesis of carbon-coated Co_3O_4 nanoneedle arrays (Co_3O_4@C NNAs)

The porous Co_3O_4 NNAs are grown directly on a Ni foam substrate via a modified hydrothermal method according to our previous work.[20] In a typical synthesis, 1.16 g of $Co(NO_3)_2\cdot 6H_2O$, 0.60 g of NH_4F and 1.20 g of urea were successively dissolved into 80 mL of deionized water at room temperature under stirring for 30 min. After that, the above prepared aqueous solution and a piece of pretreated Ni foam (~3×8 cm^2) were transferred into a 100 mL Teflon-lined stainless-steel autoclave, which was sealed and maintained at 120 °C for 9 h in oven. After the reaction, the sample was collected and washed with deionized (DI) water for several times. Finally, the precursor was annealed at 400 ^{o}C for 4 h in air with a ramping temperature rate of 2 ^{o}C min^{-1}, black color crystallized Co_3O_4 NNAs on Ni foam was obtained after annealing. To fabricate carbon-coated Co_3O_4 NNAs, one piece of the as-prepared Co_3O_4/Ni foam substrate was first immersed into a 0.04 M aqueous glucose solution for 12 h, followed by carbonization at 450 °C in a tube furnace under Ar gas protection for 2 h, resulted in Co_3O_4@C core-shell NNAs.

Preparation of Co_3O_4@C@Ni_3S_2 core-shell-shell hybrid nanoneedle arrays (Co_3O_4@ C@Ni_3S_2 NNAs)

In a typical synthesis, 4.5 mM $Ni(NO_3)_2 \cdot 6H_2O$ and 4.5 mM thiourea were dissolved in 80 mL DI water by magnetic stirring. The resulting homogeneous solution and a piece of Ni foam with Co_3O_4@C NNAs were transferred into a 100 mL Teflon-lined stainless steel autoclave, sealed and kept at 120 ^{o}C for 3 h for hydrothermal growth. After the reaction, the as-obtained Co_3O_4@C@Ni_3S_2 NNAs sample was washed thoroughly by DI water and dried in vacuum oven for 5 h at 60 ^{o}C. To investigate the formation process, the intermediate products were collected by varying the precursor concentration with 1.5 mM, 3.0 mM, 4.5 mM and 6.0 mM. In addition, the bare Ni_3S_2 nanoflakes and the Co_3O_4@Ni_3S_2 NNAs on Ni foam were also synthesized through a similar approach. The chemical reaction equations for the second hydrothermal fabrication process can be expressed as follows [27, 32]:

$$(NH_2)_2CS + 2H_2O \rightarrow H_2S + CO_2 + 2NH_3 \qquad (1)$$

$$H_2S + H_2O \rightarrow HS^- + H_3O^+ \qquad (2)$$

$$2HS^- + Ni^{2+} + 2Ni \rightarrow Ni_3S_2 + H_2 \qquad (3)$$

Materials characterization

The morphology was measured by a field-emission scanning electron microscopy (SEM) (JSM-7600F microscope, Japan), transmission electron microscopy (TEM) and high resolution TEM (HRTEM) (JEOL JEM-2010). Energy dispersive X-ray spectroscopy (EDS) analyses were performed using a JSM-7600F microscope (Japan). The crystal structure of the as-synthesized products was characterized by a Bruker D8 Advance Eco X-ray powder diffractometer (XRD) with Cu-Ka radiation (λ=1.5418 Å) in the 2θ range of 10°~80°. Raman spectroscopy was carried out using a WITEC CRM200 Raman system equipped with a 532 nm laser source. The mass loading of the active material was carefully weighed on a microbalance with an accuracy of 0.01 mg (AUW120D, Shimadzu, Japan).

Electrochemical measurement based on three-electrode supercapacitors testing configuration

The electrochemical tests were conducted by an electrochemical workstation (VMP3, Bio-Logic, France) with a typical three-electrode cell with the as-prepared sample as the working electrode, Pt foil as the counter electrode and, Ag/AgCl electrode as the reference electrode, and 3 M KOH as the electrolyte. Cyclic voltammery (CV) tests were measured between -0.2 and 0.6 V at various scan rates ranging from 5 to 100 mV s^{-1} at room temperature. The galvanostatic charge/discharge tests were conducted between -0.05 and 0.45 V at various current densities of 1-30 mA cm^{-2}. The electrochemical impedance spectroscopy (EIS) measurements were performed by applying an alternate current voltage with 5 mV amplitude in a frequency range from 0.01 Hz to 100 kHz at open circuit potential. The nominal area of the sample immersed into the electrolyte is controlled to be around 1.5×2.0 cm^2. Areal capacitances were calculated from the discharge curves according to $C_a=I\times\Delta t/(\Delta V\times S)$, where I is the constant discharge current, Δt is the discharging time, ΔV is the voltage drop upon discharging (excluding the IR drop), and S is the geometrical area of the electrode.

Electrochemical measurement of the all-solid-state asymmetric supercapacitors device

To fabricate an all-solid-state asymmetric supercapacitor, a Co_3O_4@C@Ni_3S_2 NNAs electrode, activated carbon (AC) electrode and PVA-KOH polymer were used as the positive electrode, negative electrode and gel electrolyte, respectively. The negative electrode was prepared as follows: first, AC, acetylene black and polyvinylidene fluoride (PVDF) in a mass ratio of 80:10:10 were dispersed in *N*-methylpyrrolidinone (NMP) to produce a homogeneous slurry. Then the resulting mixture was coated onto Ni foam substrate (1.5×4.0 cm^2) using a spatula. Finally, the fabricated electrode was pressed and dried under vacuum at 80 ^oC for 6 h. PVA-KOH gel electrolyte was used as both the ionic electrolyte and separator, which was prepared as follows: 6 g of PVA was dissolved in 60 mL DI water with stirring at 100 ^oC for 2 h. After that, 3 g of KOH was dissolved in 20 mL DI water. Above two solutions were mixed together at 90 ^oC under vigorous stirring until the solution become clear. Then, two pieces of electrode were immersed into the PVA-KOH solution for 10 min. The final all-solid-state supercapacitor was prepared by assembled two electrodes until PVA-KOH gel solidified and excess water evaporated. The cyclic voltammetry (CV) and galvanostatic charge-discharge tests were performed between 0 and 1.8 V at various scan rates (3-100 mV s^{-1}) and in different current densities (2-20 mA cm^{-2}), respectively. The nominal area of the sample immersed into the gel electrolyte is controlled to be around 1.5×4.0 cm^2.

3. Results and discussion

The synthesis processes of highly ordered Co_3O_4@C@Ni_3S_2 nanoneedle arrays on Ni foam are schematically illustrated in Figure 1. The synthesis procedure of nanoneedle arrays was summarized briefly in four steps: first, porous Co_3O_4 nanoneedle arrays were grown on nickel foam substrate via a hydrothermal synthesis process (step (i) and step (ii)). And then the as-obtained porous nanoneedles are subjected to impregnation with glucose aqueous solution and subsequent post-annealing in Ar gas, resulting in a uniform coating of an amorphous carbon layer on the Co_3O_4 NNAs surface (step (iii)). Finally, the Co_3O_4@C NNAs was soaked in a mixed solution ($Ni(NO_3)_2$ and thiourea, with mole ratio of (1:1) to prepare the final Co_3O_4@C@Ni_3S_2 core-shell-shell hybrid nanoneedle arrays (step (iv)). In the ternary composite of Co_3O_4@C@Ni_3S_2, carbon was chosen as the intermediate layer because it is capable of performing charge storage by a fast redox reaction. Moreover, the electrical conductivity of carbon (amorphous; $10\text{-}10^3$ S cm^{-1}) is much higher than that of Co_3O_4 ($10^{-4}\text{-}10^{-2}$ S cm^{-1}), thus the carbon layer can provide an effective path way for fast electron transport and accelerates the reaction kinetics between electroactive center and current collector[33, 34]. Furthermore, the carbon layer also can protect the Co_3O_4 nanoneedle array structure.

The surface morphology and hierarchical structure of the as-synthesized nanostructures were characterized by scanning electron microscopy (SEM). Figure 2a show the SEM images of Co_3O_4 NNAs on Ni foam with different magnifications. It can be seen that dense and aligned Co_3O_4 NNAs are uniformly covered on the nickel foam skeletons. The magnified image (inset of in Figure 2a) reveals that they are highly mesoporous with a diameter of about 80 nm at the middle section, which may result from the release of CO_2 gas during the thermal decomposition process (step (ii) in Figure 1). After the glucose hydrothermal reaction and subsequent heat treatment, the Co_3O_4 nanoneedle core is well wrapped by one layer of amorphous carbon, forming Co_3O_4@C core-shell nanoneedles (see Figure 2b). The diameter of Co_3O_4@C nanoneedle is increased from the tip to the fixed end without obvious change of the surface morphology. As shown in Figure 2c-d, ultrathin (< 50 nm) hexagonal Ni_3S_2 nanoflakes with typical diameters of 0.5~1.0 μm are interconnected with Co_3O_4@C NNAs after the second hydrothermal treatment. Moreover, the underlying tips of Co_3O_4@C can still be observed indicated by dashed circles in Figure 2d, which further illustrate the nanoneedle arrays are still well maintained. The pores or voids between nanoneedles and nanoflakes act as effective transportation channels for the electrolyte during the charge-discharge process. The length of individual Co_3O_4@C@Ni_3S_2 nanoneedle is about 4 μm in length by a closer observation as shown in Figure 2f. At the same time, the morphology of pure Ni foam, Ni_3S_2 nanoflakes and Co_3O_4@Ni_3S_2 NNAs are also shown in Figure S2. After the acid treatment for removing the possible impurities/oxide layer on the surface of Ni foam, a flat and clean surface is clearly shown in Figure S2a and S2b. Ni_3S_2 nanoflakes are uniformly grown on the surface of nickel foam skeleton as shown in Figure S2c and S2d. The thickness of the hexagonal Ni_3S_2 nanoflakes is about 60 nm with the width ranging from 2 to 3 μm (inset of Figure S2c). As illustrated in Figure S2e and S2f, the morphologies of the Co_3O_4@Ni_2S_3

NNAs are well retained, but with much collapse. In these unique designed nanostructures, the carbon coating provides dual functionality: first, it significantly enhances the electron transport throughout the composite materials; second, it protects the morphology of Co_3O_4 nanoneedle arrays from damage in the second hydrothermal reaction process.

The detailed microstructure of the sample at different stages was performed by transmission electron microscopy (TEM) and high-resolution TEM (HRTEM). The needle-like nanostructure of Co_3O_4 arrays are composed of Co_3O_4 nanocrystallites with a size of 10-15 nm and small gap of about 2-5 nm, as shown in Figure 3a. As shown in Figure 3b, the lattice spacing of ca. 0.24 nm, 0.27 nm and 0.47 nm corresponds to the (311), (200) and (111) planes of Co_3O_4. In addition, the corresponding selected area electronic diffraction (SAED) pattern of Co_3O_4 NNAs shows a set of well-defined spots, indicating its single-crystallinity property (inset of Figure 3b). The TEM and HRTEM of Co_3O_4@C NNAs shown in Figure 3c and 3d clearly display the core-shell structures of Co_3O_4/C nanoneedle. The. amorphous carbon layer has a uniform thickness of about 5~8 nm, creating a smooth, highly conductive layer over the entire nanoneedles surface as indicated in Figure 3d. Figure 3e and 3f show the typical TEM images of the Co_3O_4@C@Ni_3S_2 NNAs taken at different magnifications. Mesoporous Co_3O_4@C “nanocore” is tightly bonded and totally covered with hexagonal-like ultrathin Ni_3S_2 nanoflakes, forming a typical core-shell-shell heterostructure. The inset of Figure 3e and Figure 3f is the HRTEM images collected from the square area 1 and 2 in Figure 3e, respectively. The lattice spacing of 0.28 nm is the (110) interplanar distance of orthogonal Ni_3S_2 phase. Furthermore, the HRTEM analysis and related fast Fourier transform (FFT) pattern reveal that the Ni_3S_2 nanoflake is single crystalline. The thickness of the Ni_3S_2 nanoflakes is ~10 nm.

The phase and structures of as prepared nanostructures are carried out by powder X-ray diffraction (XRD) and Raman spectrum. As seen from Figure 4a, all diffraction peaks of the needle-like Co_3O_4 arrays specimen could be well indexed with cubic phase Co_3O_4 (JCPDS card no. 42-1467).[20] The other distinct diffraction peaks located at 21.7, 31.1, 37.7, 50.1 and 55.11 degree can be indexed to the (010), (**Error! Reference source not found.**10), (111), (-120) and (-121) planes of Ni_3S_2 (JCPDS card no. 85-1802), respectively.[35] The three strongly peaks marked by "#" belong to the Ni substrate, and the wide peak centered at ~26° (marked by "&") indicates the existence of amorphous carbon layer. No residues or contaminants have been detected, indicating high purity of these samples. The structural features of Co_3O_4@C@Ni_3S_2 nanostructures were further confirmed by Raman measurements. As shown in Figure 4b, there are five well-defined Raman peaks located at 197, 484, 523, 621 and 691 cm^{-1}, corresponding to F^3_{2g}, E_g, F^1_{2g}, F^2_{2g} and A_{1g} modes of crystalline Co_3O_4, respectively, in agreement with the previous reports.[36] Raman peaks located at 200, 222, 305, 324, and 350 cm^{-1} can be attributed to the vibration modes of orthogonal Ni_3S_2.[37] In addition, the $Co_3O_4@C@Ni_3S_2$ nanoneedle is also clearly verified by energy dispersive X-ray spectroscopy (EDS) elemental mapping analysis of Ni, Co, O, C and S (as shown in Figure 4c), in which Co and O are located in the core-region while Ni and S are distributed homogeneously at the whole nanowires shell. The EDS spectrum (Figure 4d) also indicates the incorporation of carbon layer between Ni_3S_2 shell and Co_3O_4 core.

The evolution process of Ni_3S_2 nanostructures with varied hydrothermal synthesis temperatures and concentrations of aqueous solution used in the second hydrothermal process are investigated. With a lower growth temperature of 90 °C, the morphology of as-obtained products is mainly small nanoflakes, due to the lower interfacial nucleation energy on the surface of $Co_3O_4@C$ NNAs (as shown in Figure 5a, b and Figure S3a). Figure 5c, d show the morphology of hexagonal-like Ni_3S_2 nanoflakes grown at 120 °C. The high-magnification SEM image in inset of Figure 5c shows the uniform coverage of the surfaces of the $Co_3O_4@C$ NNAs by Ni_3S_2 nanoflakes, which are interconnected with each other to form a porous surface. When the synthesis process was carried out at a higher temperature (150 °C), large and ruleless Ni_3S_2 nanosheets were obtained (Figure 5e, f and Figure S3b). The morphology change of Ni_3S_2 with increased growth temperature maybe due to the slow decomposition rates of thiourea at a higher temperature, as a result in affecting the nucleation growth process of Ni_3S_2.[38] The TEM observation (inset of Figure S3a, b) further demonstrates the uniformity coverage of the Ni_3S_2 nanoflakes or nanosheets, with the thickness of 20~40 nm for Ni_3S_2 nanoflakes and 10~20 nm nanosheets layer. Moreover, all the Ni_3S_2 nanostructures prepared at various growth temperatures are orthogonal phase evidenced by XRD patterns and Raman spectra (Figure S3c, d).

The loading of Ni_3S_2 nanoflakes on $Co_3O_4@C$ NNAs can be tailored by changing the aqueous mixed solution (AMS, $Ni(NO_3)_2$ and thiourea) at 1.5, 3.0, 4.5 and 6.0 mM. Figure S4 shows the $Co_3O_4@C@Ni_3S_2$ nanostructures morphologies changes with various concentrations of AMS. Nanoflakes were irregularly attached on the nanoneedles at low AMS (1.5 mM) (as shown in Figure S4a). As the concentration of aqueous mixed solution increased, the loading amount of the Ni_3S_2 nanoflakes increased (Figure S4b-d). At high concentration of AMS, nanoflakes densely wrapped the nanoneedles and Ni foam skeleton, as shown in Figure S4d. The proposed growth mechanism is summarized in Figure S4e. Based on the nucleation and growth theory, the solution was filled with enough monomers for heterogeneous nucleation, inducing nanoflakes thoroughly and uniformly covered on the nanoneedles skeletons, and the nucleated Ni_3S_2 nanoflakes on the nanoneedle was uniformly grown by sufficient monomers.[39] Therefore, fast heterogeneous nucleation and moderate growth rates by adjusting the synthesis temperature and precursor concentration are essential for growing uniform and regular nanoflakes on one-dimensional Co_3O_4@C nanoneedles backbones.

To evaluate the electrochemical performance of the synthesized nanostructures, electrochemical measurements were performed by a three-electrode system with 3 M KOH aqueous electrolyte, a platinum foil counter electrode and an Ag/AgCl reference electrode. Figure S5a shows the cyclic voltammetric (CV) curves of the Co_3O_4@C@Ni_3S_2 nanostructure arrays that prepared under various temperatures (e.g. 90 °C, 120 °C and 150 °C). The tests were carried out at a scan rate of 30 mV s^{-1} in the potential range from -0.2 to 0.6 V (vs. Ag/AgCl). The CV curve of the Co_3O_4@C@Ni_3S_2 NNAs prepared at 120 °C had the largest integrated area compared to that the other two electrodes, indicating the highest specific capacitance for Co_3O_4@C@Ni_3S_2 NNAs growth at 120 °C. Figure S5b depicts the results of galvanostatic charge-discharge measurements on the three different core-shell-shell composite electrodes with a constant applied current density of 3 mA cm^{-2}, the charge-discharge time of the Co_3O_4@C@Ni_3S_2 NNAs obtained at 120 °C is the longest for the three samples. In addition, the CV and galvanostatic charge-discharge curves of the hierarchical Co_3O_4@C@Ni_3S_2 NNAs obtained at various concentrations of AMS for 120 °C in Figure S5c and S5d show demonstrate that the Co_3O_4@C@Ni_3S_2 NNAs obtained at 4.5 mM AMS processes the highest capacitance and longest discharging times. According to the above results, the following performance tests and discussion were focused on the Co_3O_4@C@Ni_3S_2 NNAs obtained at both 120 °C and 4.5 mM AMS, respectively.

Figure 6a shows a comparison on CV curves of pure Ni foam, Ni_3S_2 nanoflakes, Co_3O_4 NNAs, Co_3O_4@C NNAs, Co_3O_4@Ni_3S_2 NNAs and Co_3O_4@C@Ni_3S_2 NNAs electrodes at a scan rate of 30 mV s^{-1}. The CV integrated area of pure Ni foam is almost negligible compared with that of the other five electrodes, revealing the almost no capacitance contribution from the current collector. For the Ni_3S_2 nanoflakes electrode, a pair of well-defined redox peaks is visible, which can be attributed to the reversible redox reactions of $Ni_{(II)} \leftrightarrow Ni_{(III)}$ as shown below[40, 41]:

$$Ni_3S_2 + 3OH^- \leftrightarrow Ni_3S_2(OH)_3 + 3e^- \qquad (4)$$

Furthermore, pristine Co_3O_4 electrode exhibits two pairs of current peaks at 0.25 V and 0.45 V, which could be ascribed to the redox reaction of Co^{2+}/Co^{3+} and Co^{3+}/Co^{4+} associated with OH^- anions, respectively[40]. The reaction could be presented as follows [42, 43]:

$$Co_3O_4 + OH^- + H_2O \leftrightarrow 3CoOOH + e^- \qquad (5)$$

$$CoOOH + OH^- \leftrightarrow CoO_2 + H_2O + e^- \qquad (6)$$

After carbon coating on the surface of Co_3O_4 NNAs, CV curve of Co_3O_4@C NNAs electrode expands slightly. The emergence of two couples of redox peaks is derived from the superposition of pristine Co_3O_4 and carbon layer. Markedly, after growth of Ni_3S_2 shell, the CV curve of the Co_3O_4@C@Ni_3S_2 NNAs electrodes have drastically expanded, indicating a much larger capacitance. It should be attributed to the ultrathin Ni_3S_2 nanoflakes not only restrain the inside core NNAs from reaction with OH^-, but also increase the effective sites for electrochemical redox reaction. In addition, it is worth mentioning that the Co_3O_4@Ni_3S_2 NNAs electrodes exhibited larger capacitance than that of pristine Ni_3S_2 nanoflakes, Co_3O_4 NNAs and Co_3O_4@C NNAs electrodes, but lower than the Co_3O_4@C@Ni_3S_2 NNAs electrodes, which could be due to the structure of Co_3O_4@Ni_3S_2 arrays were collapsed at the second hydrothermal synthesis process without carbon layer protecting. As shown in Figure 6b, galvanostatic charge-discharge measurements were further performed on the all electrodes at a constant applied current density of 10 mA cm^{-2}. Since the pristine Co_3O_4 NNAs can not be charged to 0.5 V due to the oxidation evolution reaction, a relatively small potential window range from 0.05 to 0.45 V was chosen.[44] As expected, the as-prepared Co_3O_4@C@Ni_3S_2 NNAs electrode shows much longer discharging time than the other electrodes, indicating that the Co_3O_4@C@Ni_3S_2 composite electrode has a high cell-area-specific capacitance of 2.252 F cm^{-2}, several times higher than that of the original Co_3O_4 NNAs (0.850 F cm^{-2}) and Ni_3S_2 nanoflakes (0.387 F cm^{-2}), in good consistent with the CV results shown in Figure 6a. In addition, the internal resistance (IR) of the Co_3O_4@C@Ni_3S_2 NNAs hybrid electrodes was about 0.025 V, which is lower than that of the Ni_3S_2 nanoflakes electrode (the IR drop is 0.05 V) at a high current density of 10 mA cm^{-2}, further demonstrating that the carbon nanoparticles layer can effectively reduce the overall resistance, as well as improving the charge transport and electron collection rates.

The CV curves of Co_3O_4@C@Ni_3S_2 NNAs electrode at various scan rates with a potential windows ranging from -0.2 to 0.6 V are presented in Figure 6c. The shapes of these CV curves remained virtually unchanged with the potential scan rates varied from 5 to 100 mV s^{-1}, revealing the ideal capacitive behaviors and good rate capabilities of the Co_3O_4@C@Ni_3S_2 NNAs electrode. With the scan rates increase, the cathodic peak position shifts to lower potential, which is attributed to the polarization effect.[45] The CV curves of Ni_3S_2 nanoflakes, Co_3O_4 NNAs, Co_3O_4@C NNAs and Co_3O_4@Ni_3S_2 NNAs electrodes at different scan rates (5-100 mV s^{-1}) are also shown in Figure S6a-d, respectively. Figure 6d illustrates that the galvanostatic charge-discharge curves of Co_3O_4@C@Ni_3S_2 NNAs electrode measured in the current densities from 1 to 30 mA cm^{-2}. The galvanostatic charge-discharge curves of the Ni_3S_2 nanoflakes, Co_3O_4 NNAs, Co_3O_4@C NNAs and

Co_3O_4@Ni_3S_2 NNAs electrodes are also shown in Figure S7a-d, respectively. These charging and discharging curves of the ternary electrode are highly symmetric and show fairly linear slopes between -0.05 and 0.45 V, arising from the ideal capacitance behavior and fast Faraday reaction. The current density dependence of the areal capacitance for the Ni_3S_2 nanoflakes, Co_3O_4 NNAs, Co_3O_4@C NNAs and Co_3O_4@Ni_3S_2 NNAs electrodes are compared in Figure 6e. It can be found that the discharge areal capacitance of the Co_3O_4@C@Ni_3S_2 NNAs electrode is 3.564 F cm^{-2} at 1 mA cm^{-2}, which is nearly three times as that of the Co_3O_4 NNAs (1.202 F cm^{-2}) and about seven times as that of Ni_3S_2 nanoflakes (0.546 F cm^{-2}), respectively.

The intrinsic electrochemical and kinetic mechanism of the hybrid electrode was further analyzed by the electrochemical impedance spectroscopic (EIS) studies. Figure 6f illustrates the Nyquist plots of EIS spectra of all electrodes in the frequency range from 10 kHz to 0.01 Hz. An equivalent circuit (inset in Figure S8b), including the ohmic resistance (R_e), the charge transfer resistance (R_{ct}), the Warburg impedance (Z_w), the double-layer capacitance (CPE), has been adopted to simulate the experimental data. In the low-frequency area, the inclined line represents the Warburg (W) impedance corresponding to the electrolyte diffusion in porous electrode and proton diffusion in host materials.[46, 47] The Co_3O_4@C@Ni_3S_2 NNAs electrode has the largest slope in all electrodes, indicating its best capacitive performance with lower diffusion resistance. This can be attributed to the decoration of Ni_3S_2 nanoflakes with large surface area and thus facilitates the supply of OH^- to the entrance of Co_3O_4 nanopores and nickel foam microspores. In high frequency area, the intercept to x axis represents the bulk resistance of the electrochemical system (R_e), and the semicircle corresponds to the parallel combination of double-layer capacitance (CPE) and charge-transfer resistance (R_{ct}) at the working electrode-electrolyte interface.[47] Compared to the pure Co_3O_4 NNAs electrode, Co_3O_4@C NNAs has a smaller R_e (1.48 Ω vs 1.78 Ω), due to the carbon layer shell increases the electrical conductivity and the electrical contact of Co_3O_4 with nickel foam. However, after Ni_3S_2 integration, the hybrid structure have a large R_e (1.56 Ω) and R_{ct}, which mainly due to the poor electrical conductivity of Ni_3S_2.

The cycling stability plays a key role in supercapacitor applications. Cycling life tests over 5000 cycles for the different Co_3O_4@C@Ni_3S_2 core-shell-shell nanostructure arrays (e.g. 90 °C, 120 °C and 150 °C), Co_3O_4@Ni_3S_2 NNAs, Co_3O_4@C NNAs, Co_3O_4 NNAs and Ni_3S_2 nanoflakes were carried out at a current density of 10 mA cm^{-2} as shown in Figure S8a. At the same current density, Co_3O_4@Ni_3S_2 NNAs, Co_3O_4@C NNAs, Co_3O_4 NNAs and Ni_3S_2 nanoflakes can keep the capacitance retention of 66.7, 86.3, 73.4 and 77.2% after 5000 cycles, respectively. Impressively, the Co_3O_4@C@Ni_3S_2 NNAs obtained at 120 °C, has the highest capacitance retention of 92.4% with 2.081 F cm^{-2} after 5000 cycles. Moreover, the Co_3O_4@C@Ni_3S_2 NNAs have a higher initial capacitance of 2.252 F cm^{-2} in contrast to that of the hybrid Co_3O_4@Ni_3S_2 core-shell arrays (1.750 F cm^{-2}) and better cycling performances (66.7% for Co_3O_4@Ni_3S_2). The enhanced performance can be attributed to the carbon layer to prevent the Co_3O_4 structural collapsed during the bulk redox reaction. Figure S8b shows the Nyquist plots of the Co_3O_4@C@Ni_3S_2 NNAs synthesized at 120 °C after the 1st and 5000th cycles, and the equivalent circuit is shown in the inset of Figure S8b. The charge transfer resistance (R_{ct}) increases slightly from the 1st to the 5000th cycle owing to the good contact among the core-shell-shell arrays between the current-collector and core-shell-shell arrays. As shown in Figure S8c, for the Co_3O_4@C@Ni_3S_2 NNAs synthesized at 120 °C, the negligible changes shown by the last ten cycles of the test compared to the first ten cycles further demonstrates the excellent long-term cycling capability of the core-double-shell composite electrode. Meanwhile, the hierarchical structure of the hybrid nanoneedle arrays is well maintained after 5000 cycles, as shown in Figure S8d. It is also found that the thickness of Ni_3S_2 nanoflakes is increased from 55 nm to 80 nm (inset of Figure S8d), indicating nanoflakes can well accommodate volume expansion and contraction during charge-discharge cycles. [48]

To further explore the practical applications of this design, an all-solid-state asymmetric supercapacitor was assembled using the Co_3O_4@C@Ni_3S_2 NNAs electrode as the positive electrode and the activated carbon (AC) electrode as the negative electrode with the Polyvinyl alcohol (PVA)/KOH as gel electrolyte (denoted as Co_3O_4@C@Ni_3S_2//AC ASC). In contrast to liquid-based supercapacitors, solid-state device has several advantages such as flexibility, ease of fabrication, large working temperature and improved safety. A schematic diagram of the ASC is shown in Figure 7a. As shown in Figure 7b and 7c, the as-prepared supercapacitor can endure the folding without destroy its construction indicating the high flexibility. As for the ASC, the charge balance should follow the relationship of $q^+ = q^-$, and thus the mass balance between the negative electrode and positive electrode will follow the equation[49]: $m^-/m^+=(C^+\times\Delta V^+)/(C^-\times\Delta V^-)$, where m is the mass of electrode, C is the specific capacitance and ΔV is the potential range for the charge-discharge process, and the subscripts "+" and "-" are the positive and negative charge carriers. By referring to the specific capacitance calculated from the above CV results, ~3.6 mg of AC is required to be contained per square- centimeter of anode.

Prior to testing the Co_3O_4@C@Ni_3S_2//AC ASCs, the CV curves of both the cathode and anode were measured at a scan rate of 30 mV s^{-1} in a three-electrode system, as shown in Figure S9a. The AC anode electrode was tested in a voltage window of approximately

-1.0-0.2 V (vs. Ag/AgCl), and shows a typical characteristic of an electrical double-layer capacitor (EDLC). Furthermore, a stable potentional window was observed in the range from -0.2-0.6 V for Co_3O_4@C@Ni_3S_2 NNAs cathode, wherein a couple of well-defined pseudocapacitive peaks are present. Figure 7d and Figure S9b show the CV and charge-discharge curves collected at different voltage windows for the Co_3O_4@C@ Ni_3S_2//AC all-solid-state, respectively. Significantly, the volumetric capacitance (based on the volume of the entire device) increases from 0.74 to 1.31 F cm^{-3} when the operation voltage increases from 0.8 to 1.8 V (Figure S9c). Moreover, the high voltage range is favorable for improving the energy density. Thus, we have chosen an operation potential window of approximately 0-1.8 V to further study the electrochemical performance of the Co_3O_4@C@Ni_3S_2//AC ASCs.

Figure 7e exhibits typical CV curves of an optimized Co_3O_4@C@Ni_3S_2//AC ASC performed at the scan rates of 5, 8, 10, 20, 30, 50, 80 and 100 mV s^{-1}. The all-solid-state ASC exhibits a quasi-rectangular CV geometry, indicating an EDLC-like capacitive behavior and differing from that tested in a three-electrode electrochemical system. Even when the scan rate increases to be as high as 100 mV s^{-1}, the shape of the CV curve can still be well persevered, suggesting a desirable high-rate capability for power delivery. Galvanostatic charge-discharge curves of the Co_3O_4@C@Ni_3S_2//AC ASCs performed at various current densities are shown in Figure 7f. The discharge curves are almost symmetrical to the charge curves, indicating good capacitive behavior for the ASC device. The areal capacitance is 0.327 F cm^{-2} at a current density of 20 mA cm^{-2}, and the corresponding specific capacitance was also plotted (see Figure S9d). Cycling performance was carried out to examine the long-term cyclability shown in Figure S9e. During the cycling process at a current density of 10 mA cm^{-2}, a very small decrease of the capacitance may be due to the consumption of gel electrolyte caused by an irreversible reaction between the electrode material and the electrolyte. The first and last five charge-discharge cycles are shown in inset of Figure S9e, which good symmetry of both charge and discharge curves indicates superior capacitive behavior. Even after 5000 charge-discharge cycles, the device still maintained approximately a capacity retention of 91.43%, demonstrating the excellent cycling stability of the flake-shaped ASC.

The volumetric energy ($E_{\mathrm{ASCs,\ V}}$) and power ($P_{\mathrm{ASCs,\ V}}$) density are critical parameters to evaluate the performance of the SCs device. They are calculated from the following equations [46, 50]:

$$E_{\mathrm{ASCs,V}} = C_{\mathrm{ASCs,V}} \cdot \Delta V^2 / (2 \times 3.6) \qquad (7)$$

$$P_{\mathrm{ASCs,V}} = E_{\mathrm{ASCs,V}} \times 3600 / \Delta t \qquad (8)$$

where the V is the effective volume of the ASCs, ΔV is the operating voltage window in volts, and Δt is the discharge time. The energy and power densities (based on the total weight of active materials) of the ASC are shown in the Ragone plot in Figure 7g. Importantly, a maximum energy density of 1.52 mWh cm^{-3} at 6 W cm^{-3} and a high power density of 60 W cm^{-3} at 0.920 mWh cm^{-3} are obtained for the Co_3O_4@C@Ni_3S_2//AC ASCs device, which is much higher than other symmetrical or asymmetrical supercapacitors [51-58], as given in the same plot for comparison.

In order to explore the potential application of Co_3O_4@C@Ni_3S_2//AC ASCs as a flexible power source, the ASC is placed with a mechanical bending angle and its electrochemical performance is evaluated by the corresponding CV curves (as shown in Figure S9f). Obviously, the ASC shows perfectly overlapped CV curves and similar specific capacitance at different bending angles, indicating that the device could be bent to a large extent without degrading the performance. Moreover, we further demonstrate the practical application of the Co_3O_4@C@Ni_3S_2//AC ASCs by powering a light-emitting diode (LED) or a motar with two pieces of ASC connected in series or in parallel to provide a high output voltage of 3.6 V or much longer operating time. More interestingly, the ASCs could drive a small rotation motor (3.7 V, 0.45 W) for 4 min after 10 s of charging by a pair of AA batteries (Figure 7h$_1$, h$_2$) or power two seven-color LEDs (2.0 V, 20 mA) after charging for only 60 s (Figure 7i).

The designed hierarchical Co_3O_4@C@Ni_3S_2nanoneedle arrays electrode presents excellent electrochemical performance, which might be due to the following reasons. First, the Co_3O_4 is proposed to act as the nanowire scaffold, which can increase the accessible surface area for the redox reaction for fully utilization of electrochemically active Ni_3S_2. In the meanwhile, Co_3O_4 also acts as a good pseudocapacitive material accessed by OH^- in alkaline electrolyte. Second, the ultrathin Ni_3S_2 nanoflakes are well wrapped on the surfaces of Co_3O_4@C NNAs, providing a faster ion and electron transfer. Third, mesoporous Co_3O_4 nanoneedle arrays grown directly on current collecting substrate (Ni foam) without binder and conductive additives provide efficient electrical connection to the outer shell materials. Particularly, the additional ultrathin carbon NPs interlayer further improve the electrical conductivity, and the 3D flexible Ni foam serves as an excellent current collector and mechanical support for the deposition of nanometer sized active materials. Therefore, the unique three-dimensional core-shell-shell nanoneedles exhibit enhanced electrochemical performance with a higher discharge-charge capacity, superior rate capability, and longer cycling lifetime, which are critical for practical energy storage devices.

4. Conclusions

In summary, a novel sandwich heterostructure of Co_3O_4@C@Ni_3S_2 nanoneedle arrays was fabricated on nickel foam through a facile three-step synthesis approach. Owing to the high conductivity of the well-defined Co_3O_4@C NNAs and combination with the large surface area of Ni_3S_2 nanoflakes, the as-fabricated Co_3O_4@C@Ni_3S_2 NNAs exhibited high specific capacitances, good rate capability, and excellent cycling stability. The ternary architectures consisted of metal oxides nanowire core and the carbon nanoparticles shell decorated by metal sulfide could combine the advantages of three pseudocapacitive materials, exhibiting synergy for the enhancement of electrochemical performance. An asymmetric two-electrode supercapacitor was prepared and could drive a direct current (DC) motor after full charging. These results suggest that the Co_3O_4@C@Ni_3S_2 NNAs is a promising candidate for the high-performance flexible supercapacitors. This facile electrode design may open up new opportunities for development of other metal oxides/sulfides composites electrode for high-performance electrochemical storage devices applications.

Acknowledgements

C. W. Cheng acknowledges the financial support of 973 Program (Grant no. 2013CB632701), the National Natural Science Foundation of China (Grant no. 51202163) and the Innovation Program of Shanghai Municipal Education Commission (Grant no. 13ZZ025). This work is under the financial support of SUTD-MIT international design center (IDC) funding (IDG21400109).

Notes and references

[1] P. Simon, Y. Gogotsi, *Nat. Mater.*, 2008, **7**, 845-854.

[2] M. Winter, R. J. Brodd, *Chem. Rev.*, 2004, **104**, 4245-4569.

[3] T. Brezesinski, J. Wang, S. H. Tolbert, B. Dunn, *Nature Mater.*, 2010, **9**, 146-151.

[4] J. R. Miller, P. Simon, *Science*, 2008, **321**, 651-652.

[5] P. Simon, Y. Gogotsi, B. Dunn, *Science*, 2014, **343**, 1210-1211.

[6] Y. Zhai, Y. Dou, D. Zhao, P. F. Fulvio, R. T. Mayes, S. Dai, *Adv. Mater.*, 2011, **23**, 4828-4850.

[7] Y. Wang, S. F. Yu, C. Y. Sun, T. J. Zhu, H. Y. Yang, *J. Mater. Chem.*, 2012, **22**, 17584-17588.

[8] L. L. Zhang, X. S. Zhao, Chem. *Soc. Rev.*, 2009, **38**, 2520-2531.

[9] C. Liu, F. Li, L. P. Ma, H. M. Cheng, *Adv. Mater.*, 2010, **22**, 28-62.

[10] H. Jiang, P. S. Lee, C. Li, *Energy Environ. Sci.*, 2013, **6**, 41-53.

[11] Y. Wang, Z. X. Huang, Y. Shi, J. I. Wong, M. Ding, H. Y. Yang, *Sci. Rep.*, 2015, **5**, 9164.

[12] Z. Tang, C. H. Tang, H. Gong, *Adv. Funct. Mater.*, 2012, **22**, 1272-1278.

[13] H. B. Li, M. H. Yu, F. X. Wang, P. Liu, Y. Liang, J. Xiao, C. X. Wang, Y. X. Tong, G. W. Yang, *Nat. Commun.*, 2013, **4**, 1894.

[14] J. Ji, L. L. Zhang, H. Ji, Y. Li, X. Zhao, X. Bai, X. Fan, F. Zhang, R. S. Ruoff, *ACS Nano*, 2013, **7**,

6237-6243.

[15] S. J. Peng , L. L. Li , H. B. Wu , S. Madhavi, X. W. Lou, *Adv. Energy Mater.*, 2014, DOI: 10.1002/aenm.201401172.

[16] L. W. Mi, Q. Ding, W. H. Chen, Z. Zheng, H. W. Hou, C. T. Liu, C. Y. Shen, *RSC Adv.*, 2012, 2, 6817-6823.

[17] M. Gao, Y. Xu, J. Jiang, S. Yu, Chem. *Soc. Rev.*, 2013, **42**, 2986-3017.

[18] B. Qu, Y. Chen, M. Zhang, L. Hu, D. Lei, B. Lu, Q. Li, Y. Wang, L. Chen, T. Wang, *Nanoscale*, 2012, **4**, 7810-7816.

[19] X. Y. Yu, L. Yu, L. F. Shen, X. H. Song, H. Y. Chen, X. W. Lou, *Adv. Funct. Mater.*, 2014, **24**, 7440-7446.

[20] D. Z. Kong, J. S. Luo, Y. L. Wang, W. N. Ren, T. Yu, Y. S. Luo, Y. P. Yang, C. W. Cheng, *Adv. Funct. Mater.*, 2014, **24**, 3815-3826.

[21] D. Li, X. W. Li, X. Y. Hou, X. L. Sun, B. L. Liu and D. Y. He, *Chem. Commun.,* 2014, 50, 9361-9364.

[22] S. W. Chou, J. Y. Lin, *J. Electrochem. Soc.*, 2013, **160**, D178-182.

[23] H. H. Huo, Y. Q. Zhao, C. L. Xu, *J. Mater. Chem. A*, 2014, **2**, 15111-15117.

[24] X. W. Ou, L. Gan, Z. T. Luo, *J. Mater. Chem. A*, 2014, **2**, 19214-19220.

[25] W. Zhou, W. Chen, J. Nai, P. Yin, C. Chen, L. Guo, *Adv. Funct. Mater.*, 2010, **20**, 3678-3683.

[26] L. Mei, T. Yang, C. Xu, M. Zhang, L. B. Chen, Q. H. Li, T. H. Wang, *Nano Energy*, 2014, **3**, 36-45.

[27] X. W. Ou, L. Gan, Z. T. Luo, *J. Mater. Chem. A*, 2014, **2**, 19214-19220.

[28] W. Zhou, W. M. Chen, J. W. Nai, P. G. Yin, C. P. Chen, L. Guo, *Adv. Funct. Mater.*, 2010, **20**, 3678-3683.

[29] Q. X. Chu, W. Wang, X. F. Wang, B. Yang, X. Y. Liu and J. H. Chen, *Journal of Power Sources*, 2015, **276**, 19-25.

[30] J. P. Wang, S. L. Wang, Z. C. Huang, Y. M. Yu, *J. Mater. Chem. A*, 2014, **2**, 17595-17601.

[31] Z. C. Xing, Q. X. Chu, X. B. Ren, C. J. Ge, A. H. Qusti, A. M. Asiri, A. O. Al-Youbi and X. P. Sun, *Journal of Power Sources*, 2014, **245**, 463-467.

[32] Y. Q. Wang, F. W. Wang, F. M. Jin, Z. Z. Jing, *Ind. Eng. Chem. Res.*, 2013, **52**, 5616-5625.

[33] L. J. Han, P. Y. Tang, L. Zhang, *Nano Energy*, 2014, **7**, 42-51.

[34] M. L. Kaplan, P. H. Schmidt, C. H. Chen, *Appl. Phys. Lett.*, 1980, **36**, 867-869.

[35] D. Li, X. W. Li, X. Y. Hou, X. L. Sun, B. L. Liu, D. Y. He, *Chem. Commun.*, 2014, **50**, 9361-9364.

[36] Z. Dong, Y. Y. Fu, Q. Han, Y. Y. Xu, H. Zhang, *J. Phys. Chem. C*, 2007, **111**, 18475-18478.

[37] Z. Zhang, X. J. Liu, X. Qi, Z. Y. Huang, L. Ren, J. X. Zhong, *RSC Adv.*, 2014, **4**, 37278-37283.

[38] Z. Y. Lin, G. Waller, Y. Liu, M. L. Liu, C. P. Wong, *Adv. Energy Mater.,* 2012, **2**, 884-888.

[39] S. Park, H. W. Shim, C. W. Lee, H. J. Song, I. J. Park, J. C. Kim, K. S. Hong, D. W. Kim, *Nano Res.*, 2015, **8**, 990-1004.

[40] H. H. Huo, Y. Q. Zhao, C. L. Xu, *J. Mater. Chem. A*, 2014, **2**, 15111-15117.

[41] T. Zhu, Z. Wang, S. Ding, J. S. Chen, X. W. Lou, *RSC Adv.*, 2011, **1**, 397-400.

[42] Y. Y. Wang, Y. Lei, J. Li, L. Gu, H. Y. Yuan, D. Xiao, *ACS Appl. Mater. Interfaces*, 2014, **6**, 6739-6747.

[43] B. Wang, X. Y. He, H. P. Li, Q. Liu, J. Wang, L. Yu, H. J. Yan, Z. S. Li, P. Wang, *J. Mater. Chem. A*,

2014, **2**, 12968-12973.

[44] F. Y. Ning, M. F. Shao, C. L. Zhang, S. M. Xu, M. Wei, X. Duan, *Nano Energy*, 2014, **7**, 134-142.

[45] J. Yan, Z. Fan, W. Sun, C. Ning, T. Wei, Q. Zhang, R. Zhang, L. Zhi, F. Wei, *Adv. Funct. Mater.*, 2012, **22**, 2632-2641.

[46] L. N. Gao, F. Y. Qu, X. Wu, *J. Mater. Chem. A*, 2014, **2**, 7367-7372.

[47] L. J. Han, P. Y. Tang, L. Zhang, *Nano Energy*, 2014, **7**, 42-51.

[48] J. Y. Wan, A. F. Kaplan, J. Zheng, X. G. Han, Y. C. Chen, N. J. Weadock, N. Faenza, S. Lacey, T. Li, J. Guo, L. B. Hu, *J. Mater. Chem. A*, 2014, **2**, 6051-6057.

[49] J. H. Zhu, J. Jiang, Z. P. Sun, J. S. Luo, Z. X. Fan, X. T. Huang, H. Zhang, T. Yu, *Small*, 2014, **10**, 2937-2945.

[50] D. S. Yu, K. L. Goh, H. Wang, L. Wei, W. C. Jiang, Q. Zhang, L. M. Dai, Y. Chen, *Nat. Nanotechnol.*, 2014, **9**, 555-562.

[51] J. Xu, Q. F. Wang, X. W. Wang, Q. Y. Xiang, B. Liang, D. Chen, G. Z. Shen, *ACS Nano*, 2013, **7**, 5453-5462.

[52] J. X. Feng, S. H. Ye, A. L. Wang, X. F. Lu, Y. X. Tong, G. R. Li, *Adv. Funct. Mater.*, 2014, **24**, 7093-7101.

[53] L. Bao, X. Li, *Adv. Mater.*, 2012, **24**, 3246-3252.

[54] M. F. El-Kady, V. Strong, S. Dubin, R. B. Kaner, *Science*, 2012, **335**, 1326-1330.

[55] L. Yuan, B. Yao, B. Hu, K. Huo, W. Chen, J. Zhou, *Energy Environ. Sci.*, 2013, **6**, 470-476.

[56] X. F. Wang, B. Liu, R. Liu, Q. F. Wang, X. J. Hou, D. Chen, R. M. Wang, G. Z. Shen, *Angew. Chem. Int. Ed.*, 2014, **53**, 1849-1853.

[57] X. H. Lu, M. H. Yu, G. M. Wang, T. Zhai, S. L. Xie, Y. H. Ling, Y. X. Tong, Y. Li, *Adv. Mater.*, 2013, **25**, 267-272.

[58] P. H. Yang, Y. Ding, Z. Y. Lin, Z. W. Chen, Y. Z. Li, P. F. Qiang, M. Ebrahimi, W. J. Mai, C. P. Wong, Z. L. Wang, *Nano Lett.,* 2014, **14**, 731-736.

Figure captions

Figure 1 Schematic illustration of the fabrication process for Co_3O_4@C@Ni_3S_2 core-shell-shell nanoneedle arrays on Ni foam: (i) hydrothermal synthesis; (ii) annealing; (iii) carbon painting; (iv) the second hydrothermal synthesis.

Figure 2 Low-magnification and enlarged SEM images of Co_3O_4 NNAs (a) and Co_3O_4@C NNAs (b) on Ni foam; (c-d) Low-magnification and enlarged SEM images of Co_3O_4@C@Ni_3S_2 NNAs on Ni foam; (f) Cross-sectional SEM image of Co_3O_4@C@Ni_3S_2 NNAs.

Figure 3 Low-magnification and high-magnification TEM images of (a, b) the Co_3O_4 NNAs; (c, d) Co_3O_4@C NNAs; (e, f) Co_3O_4@C@Ni_3S_2 NNAs. The insets of (b), (e) and (f) are the corresponding SAED patterns from Co_3O_4 NNAs, Ni_3S_2 nanoflake and Co_3O_4@C@Ni_3S_2 NNAs, respectively.

Figure 4 (a) XRD patterns and (b) Raman spectra of Ni_3S_2 nanoflakes, Co_3O_4 NNAs, Co_3O_4@Ni_3S_2 NNAs, Co_3O_4@C NNAs and Co_3O_4@C@Ni_3S_2 NNAs; (c) SEM image of the Co_3O_4@C@Ni_3S_2 NNAs and EDS element maps of Ni, Co, O, C and S; (d) EDS spectrum of the hybrid Co_3O_4@C@Ni_3S_2 NNAs shown in (c).

Figure 5 SEM images of nanostructured Co_3O_4@C@Ni_3S_2 arrays synthesized at various temperatures of (a, b) 90 °C, (c, d) 120 °C, (e, f) 150 °C in the second hydrothermal process. The inserts in (b), (d) and (f) are the proposed schematic morphologies.

Figure 6 (a) Comparison of CV and (b) galvanostatic charge-discharge curves for pure Ni foam, Ni_3S_2 nanoflakes, Co_3O_4 NNAs, Co_3O_4@C NNAs, Co_3O_4@Ni_3S_2 NNAs and Co_3O_4@C @Ni_3S_2 NNAs structrures at a scan rates of 30 mV s^{-1} and a current density of 3 mA cm^{-2}, respectively; (c) CV and (d) galvanostatic charge-discharge curves of Co_3O_4@C @Ni_3S_2 nanostructures at various scan rates and current density in 3 M KOH aqueous liquid electrolyte, respectively; (e) Current density dependence of the area specific capacitance of Ni_3S_2 nanoflakes, Co_3O_4 NNAs, Co_3O_4@C NNAs, Co_3O_4@Ni_3S_2 NNAs and Co_3O_4@C@ Ni_3S_2 NNAs electrodes; (f) Nyquist plots of the pure Ni foam, Ni_3S_2 nanoflakes, Co_3O_4 NNAs, Co_3O_4@C NNAs, Co_3O_4@Ni_3S_2 NNAs and Co_3O_4@C@Ni_3S_2 NNAs electrodes at open circuit potential. The inset of (f) is the enlarged EIS of these electrodes at high frequency range.

Figure 7 (a) Schematic diagram of the all-solid asymmetric supercapacitor configuration; (b, c) Photographs of the device in normal and bending states, and the square indicates the active region; (d) CV curves of Co_3O_4@C@Ni_3S_2//AC ASC device measured at various potential windows at a scan rate of 20 mV s^{-1}; (e) CV curves of the Co_3O_4@C@Ni_3S_2//AC ASC device at various scan rates; (f) Galvanostatic charge-discharge curves of the Co_3O_4@C@Ni_3S_2//AC ASC device at various current densities; (g) Comparison in a Ragone plots of the volumetric energy densities and power densities reported in previous references and our Co_3O_4@C@Ni_3S_2//AC ASC device; (h_1, h_2) Photos of a 3×6 cm^2 ASC device drives a small motar for 4 min after 10 s of charging by a pair of AA batteries; (i) Two pictures showing that two ASCs (each one: 1.5×4.0 cm^2×0.3 cm) in series can lighten up two seven-color LED brightly.

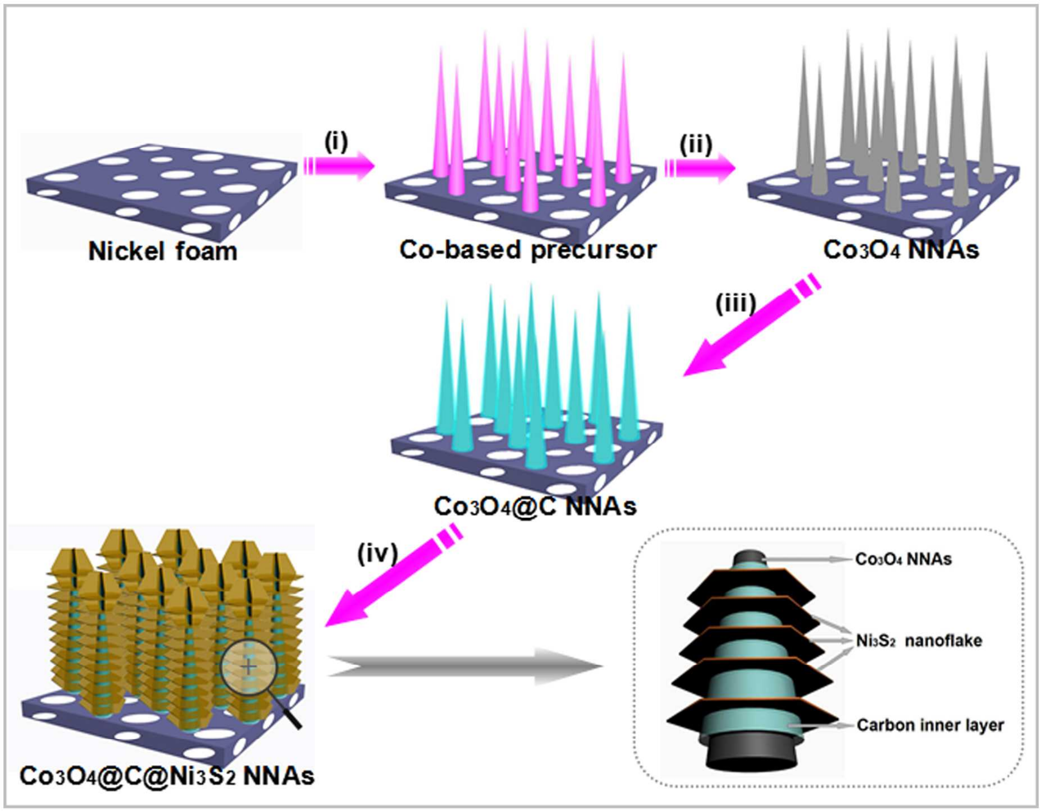

Figure 1 Schematic illustration of the fabrication process for Co_3O_4@C@Ni_3S_2 sandwich-structured nanoneedle arrays on Ni foam: (i) hydrothermal synthesis; (ii) annealing; (iii) carbon painting; (iv) the second hydrothermal synthesis.

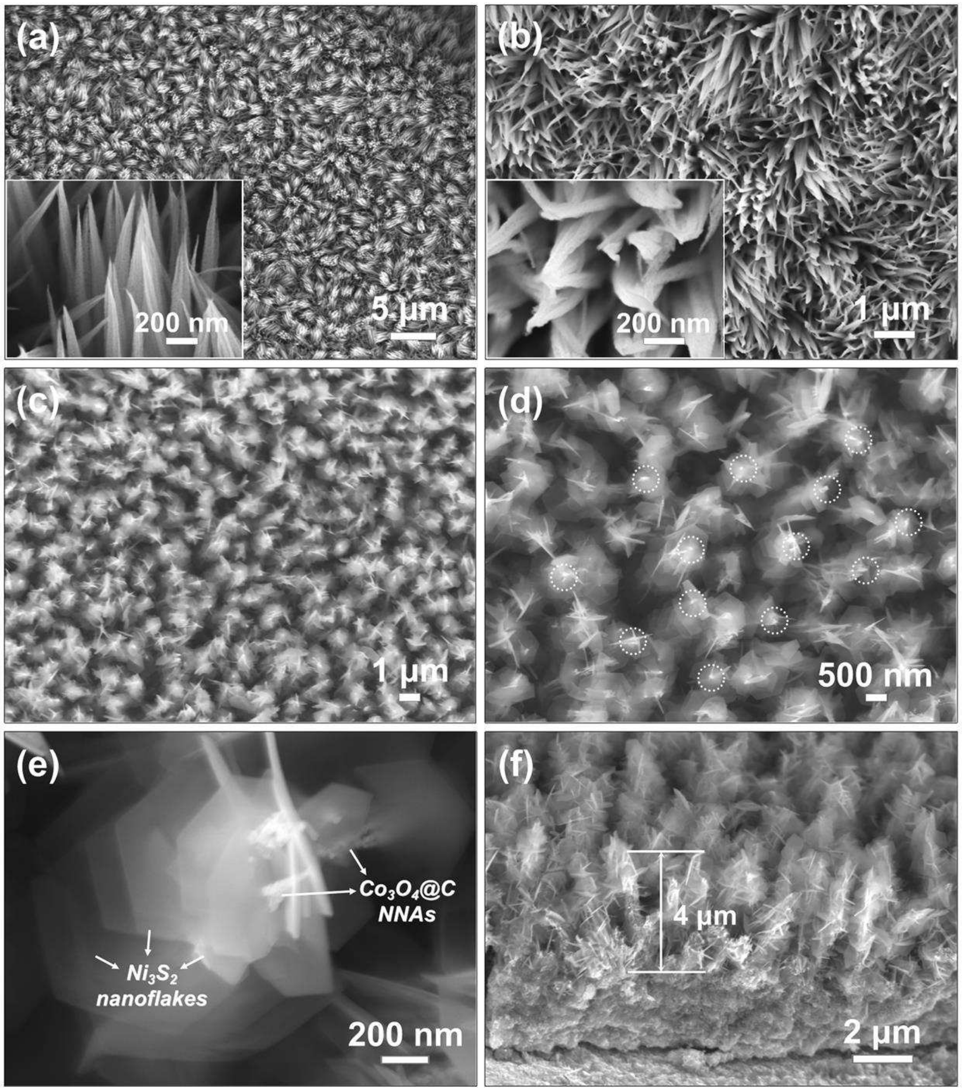

Figure 2 Low-magnification and enlarged SEM images of Co_3O_4 NNAs (a) and Co_3O_4@C NNAs (b) on Ni foam; (c-e) Low-magnification and enlarged SEM images of Co_3O_4@C@Ni_3S_2 NNAs on Ni foam; (f) Cross-sectional SEM image of Co_3O_4@C@Ni_3S_2 NNAs.

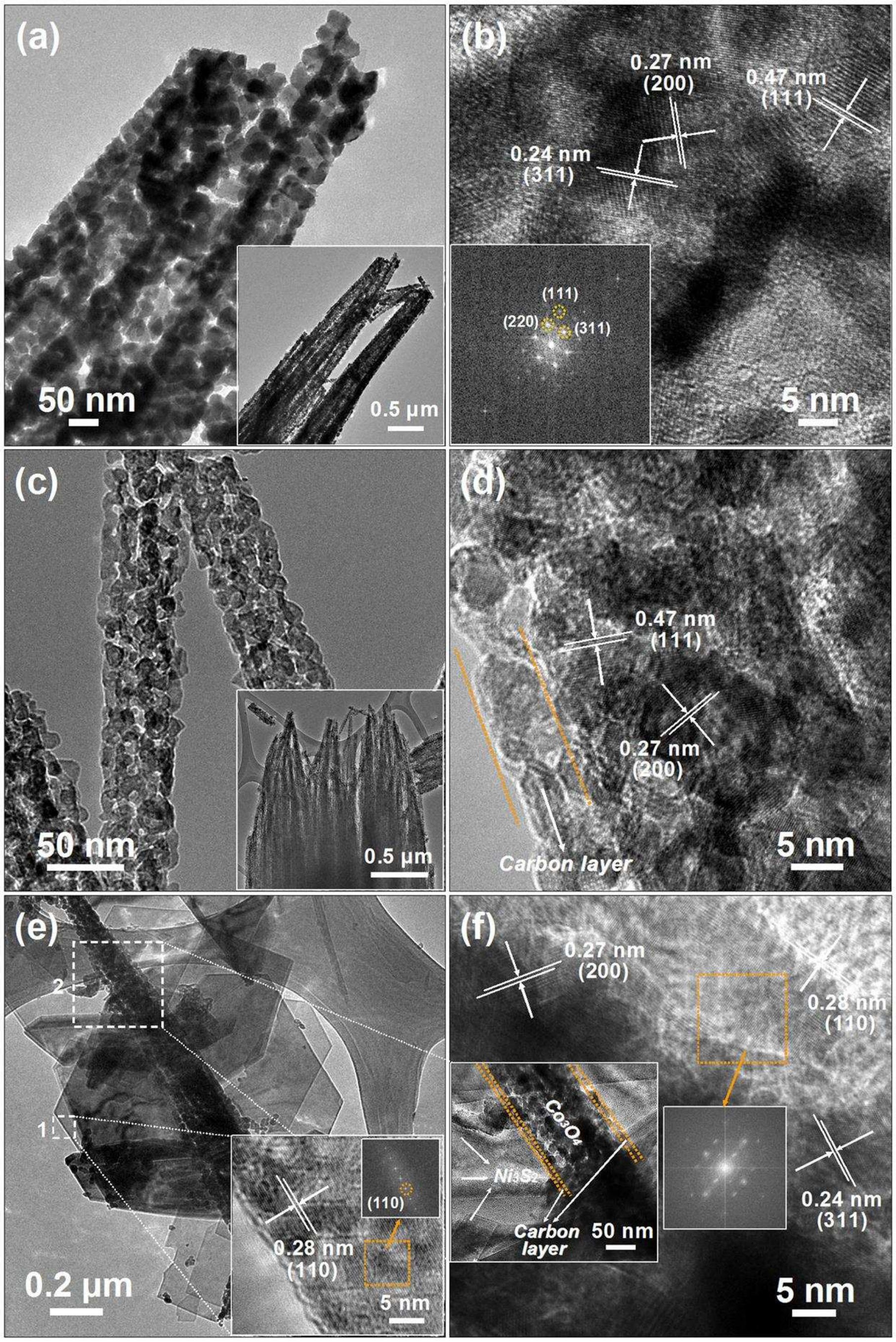

Figure 3 Low-magnification and high-magnification TEM images of (a, b) the Co_3O_4 NNAs; (c, d) Co_3O_4@C NNAs; (e, f) Co_3O_4@C@Ni_3S_2 NNAs. The insets of (b), (e) and (f) are the corresponding SAED patterns from Co_3O_4 NNAs, Ni_3S_2 nanoflake and Co_3O_4@C@Ni_3S_2 NNAs, respectively.

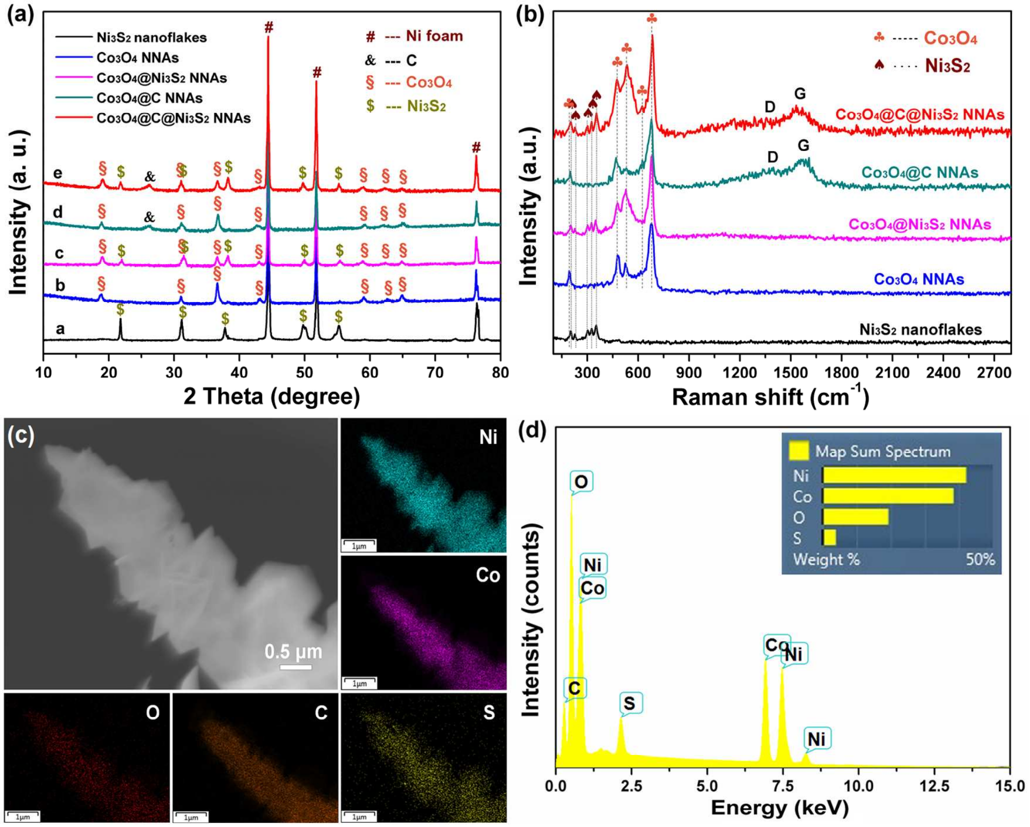

Figure 4 (a) XRD patterns and (b) Raman spectra of Ni_3S_2 nanoflakes, Co_3O_4 NNAs, Co_3O_4@Ni_3S_2 NNAs, Co_3O_4@C NNAs and Co_3O_4@C@Ni_3S_2 NNAs; (c) SEM image of the Co_3O_4@C@Ni_3S_2 NNAs and EDS element maps of Ni, Co, O, C and S; (d) EDS spectrum of the hybrid Co_3O_4@C@Ni_3S_2 NNAs shown in (c).

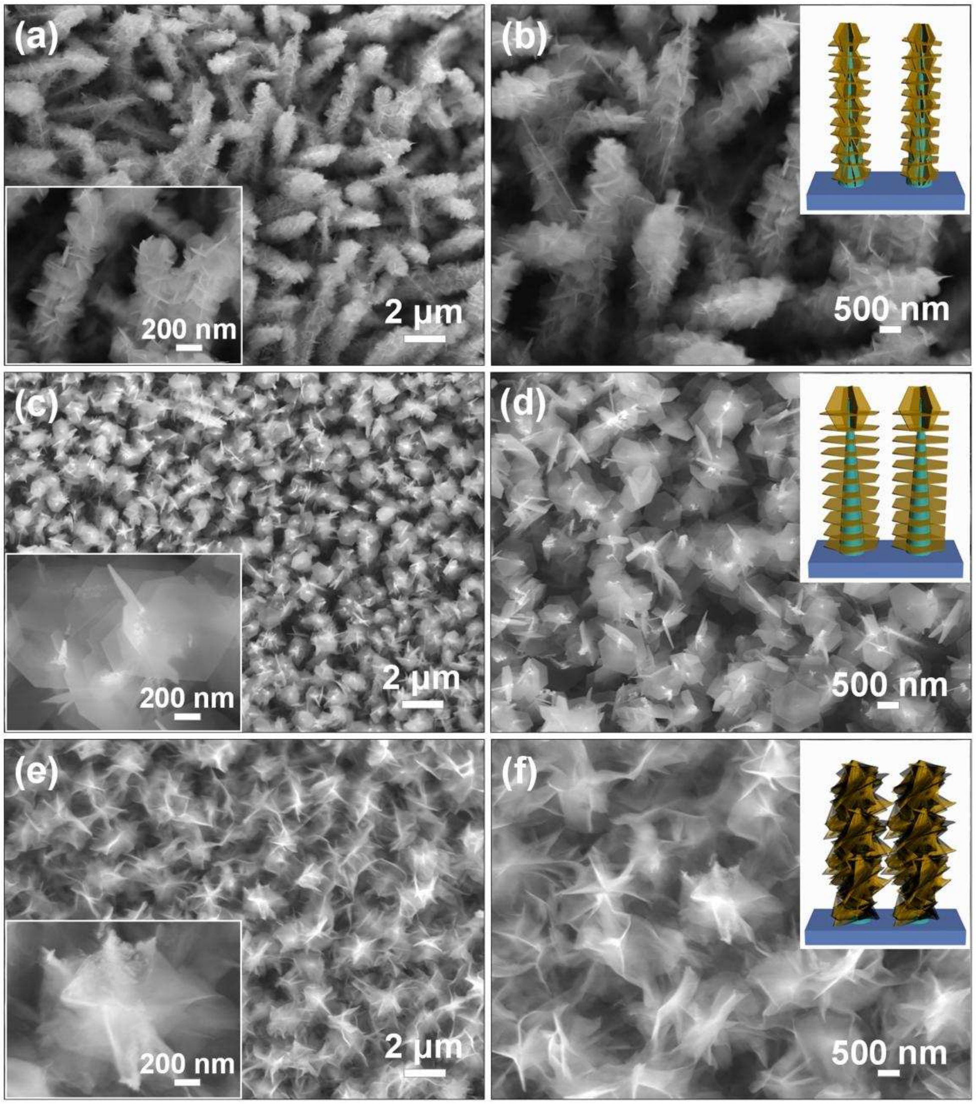

Figure 5 SEM images of nanostructured $Co_3O_4@C@Ni_3S_2$ arrays synthesized at various temperatures of (a, b) 90 °C, (c, d) 120 °C, (e, f) 150 °C in the second hydrothermal process. The inserts in (b), (d) and (f) are the proposed schematic morphologies.

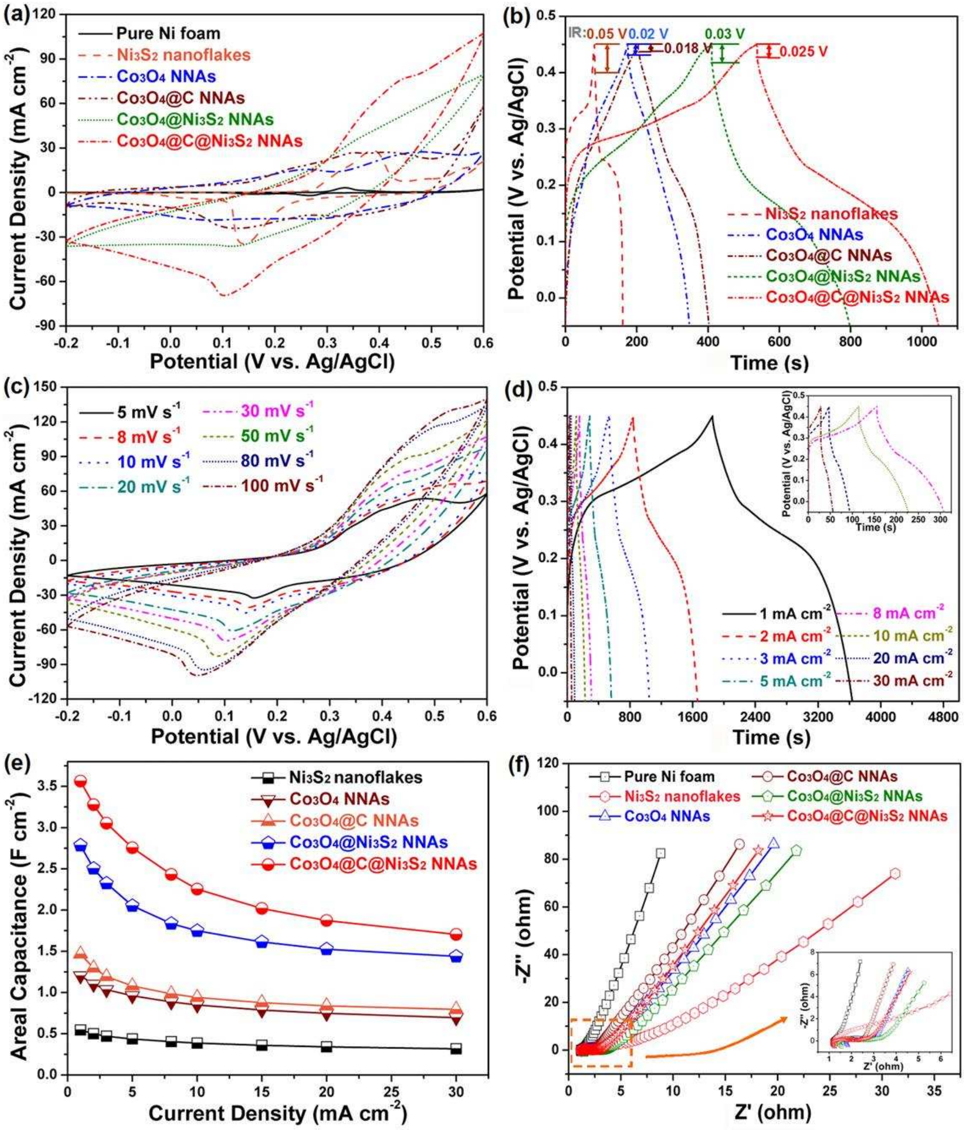

Figure 6 (a) Comparison of CV and (b) galvanostatic charge-discharge curves for pure Ni foam, Ni_3S_2 nanoflakes, Co_3O_4 NNAs, Co_3O_4@C NNAs, Co_3O_4@Ni_3S_2 NNAs and Co_3O_4@C @Ni_3S_2 NNAs structrures at a scan rates of 30 mV s^{-1} and a current density of 3 mA cm^{-2}, respectively; (c) CV and (d) galvanostatic charge-discharge curves of Co_3O_4@C@Ni_3S_2 nanostructures at various scan rates and current density in 3 M KOH aqueous liquid electrolyte, respectively; (e) Current density dependence of the area specific capacitance of Ni_3S_2 nanoflakes, Co_3O_4 NNAs, Co_3O_4@C NNAs, Co_3O_4@Ni_3S_2 NNAs and Co_3O_4@C@Ni_3S_2 NNAs electrodes; (f) Nyquist plots of the pure Ni foam, Ni_3S_2 nanoflakes, Co_3O_4 NNAs, Co_3O_4@C NNAs, Co_3O_4@Ni_3S_2 NNAs and Co_3O_4@C@Ni_3S_2 NNAs electrodes at open circuit potential. The inset of (f) is the enlarged EIS of these electrodes at high frequency range.

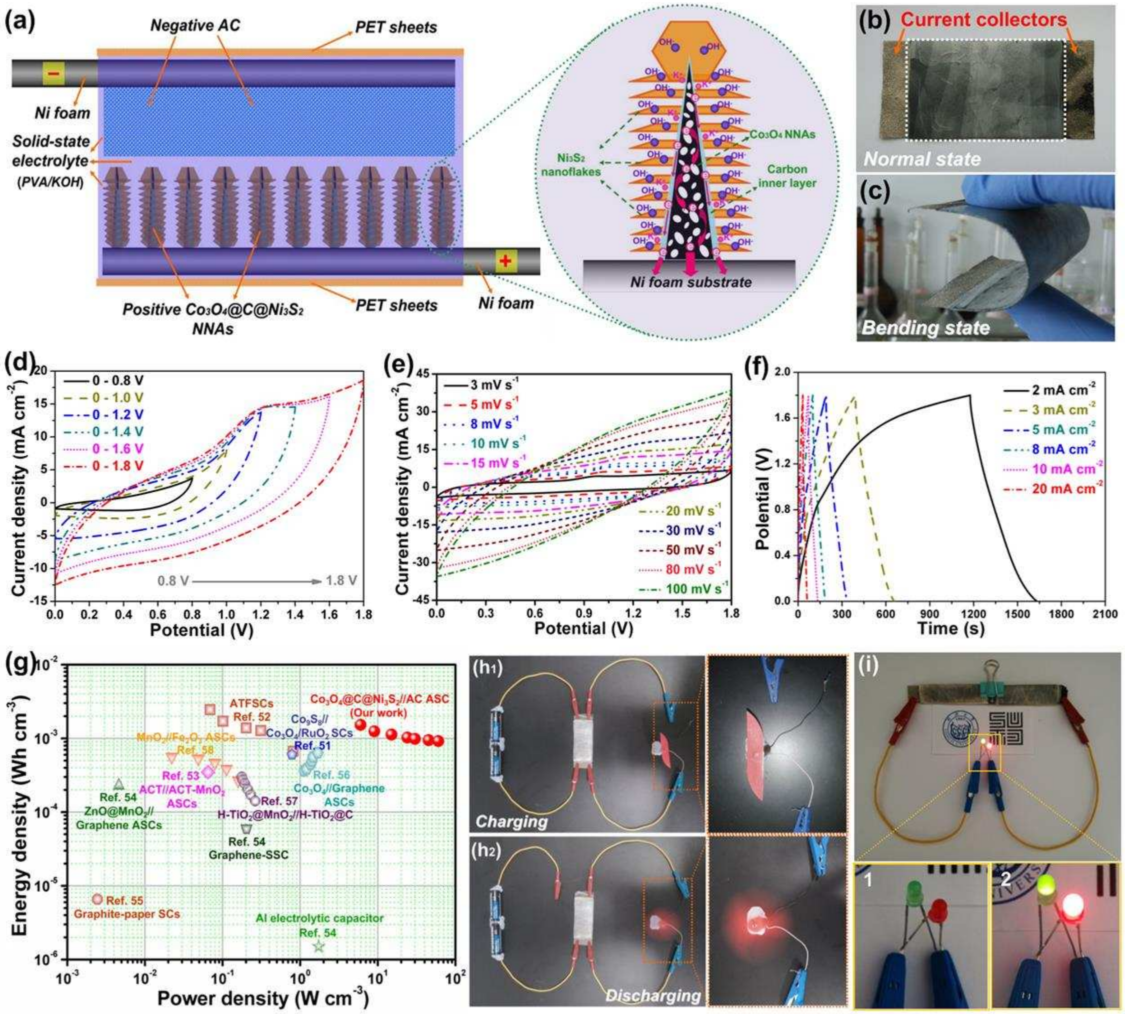

Figure 7 (a) Schematic diagram of the all-solid asymmetric supercapacitor configuration; (b, c) Photographs of the device in normal and bending states, and the square indicates the active region; (d) CV curves of Co_3O_4@C@Ni_3S_2//AC ASC device measured at various potential windows at a scan rate of 20 mV s^{-1}; (e) CV curves of the Co_3O_4@C@Ni_3S_2//AC ASC device at various scan rates; (f) Galvanostatic charge-discharge curves of the Co_3O_4@C@Ni_3S_2//AC ASC device at various current densities; (g) Comparison in a Ragone plots of the volumetric energy densities and power densities reported in previous references and our Co_3O_4@C@Ni_3S_2//AC ASC device; (h_1, h_2) Photos of a 3×6 cm^2 ASC device drives a small motar for 4 min after 10 s of charging by a pair of AA batteries; (i) Two pictures showing that two ASCs (each one: 1.5×4.0 cm^2×0.3 cm) in series can lighten up two seven-color LED brightly.

The table of contents entry

Keyword: Co_3O_4@C@Ni_3S_2, core-shell-shell, nanoneedle arrays, hierachical structure, asymmetric supercapacitor

Dezhi Kong, Chuanwei Cheng,* Ye Wang, Jen It Wong, Yaping Yang and Hui Ying Yang*

Three-dimensional Co_3O_4@C@Ni_3S_2 Sandwich-Structured Nanoneedle Arrays: Towards High-Performance Flexible All-Solid-State Asymmetric Supercapacitors

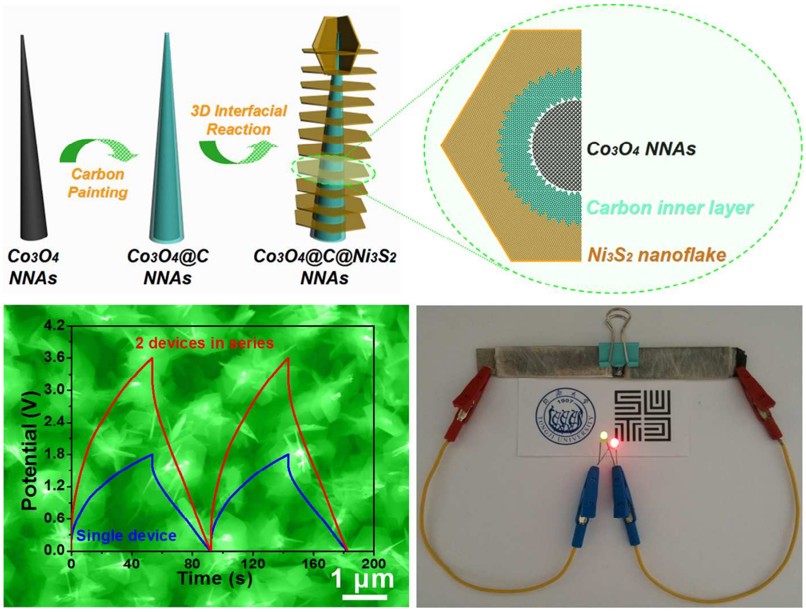

A novel asymmetric supercapacitor composed of Co_3O_4@C@Ni_3S_2 NNAs as the positive electrode and activated carbon (AC) as the negative electrode can deliver a high energy density of 1.52 mWh cm^{-3} at 6 W cm^{-3} and excellent long cycle stability, with 91.4% specific capacitance retained even after 10000 cycles.